



Published in final edited form as:

Biochemistry. 2013 September 17; 52(37): . doi:10.1021/bi400819x.

Structural Basis for Assembly of the Mn^{IV}/Fe^{III} Cofactor in the Class Ic Ribonucleotide Reductase from *Chlamydia trachomatis*†

Laura M.K. Dassama^{§,‡}, Carsten Krebs[§], J. Martin Bollinger Jr.[§], Amy C. Rosenzweig^{||}, and Amie K. Boal^{||,∇,*}

[§]Departments of Chemistry and of Biochemistry and Molecular Biology, The Pennsylvania State University, University Park PA 16802

^{||}Departments of Molecular Biosciences and of Chemistry, Northwestern University, Evanston IL 60208

Abstract

The class Ic ribonucleotide reductase (RNR) from *Chlamydia trachomatis* (*Ct*) employs a Mn^{IV}/Fe^{III} cofactor in each monomer of its α_2 subunit to initiate nucleotide reduction. The cofactor forms by reaction of Mn^{II}/Fe^{II}- α_2 with O₂. Previously, in vitro cofactor assembly from apo α_2 and divalent metal ions produced a mixture of two forms, with Mn in site 1 (Mn^{IV}/Fe^{III}) or site 2 (Fe^{III}/Mn^{IV}), of which the more active Mn^{IV}/Fe^{III} product predominates. Here we have addressed the basis for metal site-selectivity by solving X-ray crystal structures of apo, Mn^{II}, and Mn^{II}/Fe^{II} complexes of *Ct* α_2 . A structure obtained anaerobically with equimolar Mn^{II}, Fe^{II}, and apo protein reveals exclusive incorporation of Mn^{II} in site 1 and Fe^{II} in site 2, in contrast to the more modest site-selectivity achieved previously. Site-specificity is controlled thermodynamically by the apo protein structure, as only minor adjustments of ligands occur upon metal binding. Additional structures imply that, by itself, Mn^{II} binds in either site. Together the structures are consistent with a model for in vitro cofactor assembly in which Fe^{II} specificity for site 2 drives assembly of the appropriately configured heterobimetallic center, provided that Fe^{II} is substoichiometric. This model suggests that use of an Mn^{IV}/Fe^{III} cofactor in vivo could be an adaptation to Fe^{II} limitation. A 1.8 Å resolution model of the Mn^{II}/Fe^{II}- α_2 complex reveals additional structural determinants for activation of the cofactor, including a proposed site for side-on (α_2) addition of O₂ to Fe^{II} and a short (3.2 Å) Mn^{II}-Fe^{II} interionic distance, promoting formation of the Mn^{IV}/Fe^{IV} activation intermediate.

Ribonucleotide reductases (RNRs) catalyze the conversion of ribonucleotides to 2 - deoxyribonucleotides, initiating the only known pathway for nucleotide production in the de novo synthesis and repair of DNA.^{1, 2} Class I RNRs, such as the enzymes from all mammals and many aerobic bacteria and viruses, initiate nucleotide reduction with a metallocofactor,

†The coordinates of *C. trachomatis* apo and Mn^{II}/Fe^{II}- α_2 have been deposited in the Protein Data Bank with accession codes 4M1H and 4M1I.

*Corresponding author. A.K.B.: Tel: 814-867-2863, akb20@psu.edu.

Present address. Department of Molecular Biosciences, Northwestern University, Evanston, IL 60208

Present address. Departments of Biochemistry and Molecular Biology and of Chemistry, The Pennsylvania State University, University Park PA 16802

†This work was supported by NIH grants GM58515 (A.C.R.) and GM55365 (J.M.B and C.K.), an Alfred P. Sloan Foundation scholarship to L.M.K.D., and an NIH Pathway to Independence award to A.K.B.

SUPPORTING INFORMATION AVAILABLE

Supplementary tables 1-9 and additional figures. This material is available free of charge via the Internet at <http://pubs.acs.org>.

assembled and stored in each monomer of the homodimeric α_2 subunit. The metallocofactor in α_2 transiently oxidizes a Cys residue $\sim 35 \text{ \AA}$ away in a monomer of the homodimeric α_2 subunit via a reversible long-range radical-translocation (RT) process.³ The resultant Cys radical abstracts a hydrogen atom from the β -carbon of the substrate in the first step of the transformation that reduces the α -carbon.^{4, 5}

The use of different metallocofactors by the RNRs in class I is the basis for their further division into subclasses a, b, and c. Members of class Ia and class Ib employ carboxylate-bridged homodinuclear $\text{Fe}_2^{\text{III/III}}$ or $\text{Mn}_2^{\text{III/III}}$ clusters, respectively, (Figure 1A-E) in conjunction with adjacent tyrosyl radicals ($\text{Y}\cdot$ s) to generate their Cys radicals.^{3, 6-10} The orthologs from aerobically growing *Escherichia coli* (*Ec*, Ia) and *Bacillus subtilis* (*Bs*, Ib) are the most extensively studied versions of these enzymes. The homodinuclear cofactors can be formed by addition of the divalent metals to metal-free (apo) protein and reaction of the reduced metal centers with an oxidant: O_2 in the class Ia orthologs^{2, 3} and $\text{O}_2^{\cdot-}$ (generated from O_2 by a flavoprotein activase) in the class Ib orthologs.⁹ In each case, reaction with the oxidant produces a high-valent^{9, 11} intermediate that oxidizes the essential Tyr residue to yield the active metallocofactor. The only biochemically characterized representative of class Ic, the ortholog from the human pathogen *Chlamydia trachomatis* (*Ct*), has a Phe residue at the position corresponding to the $\text{Y}\cdot$ in the class Ia and Ib orthologs. In vitro, the *Ct* α_2 protein has been shown to assemble a heterodinuclear $\text{Mn}^{\text{IV}}/\text{Fe}^{\text{III}}$ cofactor in each α monomer and to use this cofactor in catalysis.¹²⁻¹⁵ The Mn^{IV} ion functionally replaces the $\text{Y}\cdot$ employed by the Ia and Ib orthologs. Analysis of available genome sequences suggests that many more ($\gg 100$) class Ic orthologs exist,¹⁶ but the ability of these additional (putative) RNRs to function with $\text{Mn}^{\text{IV}}/\text{Fe}^{\text{III}}$ cofactors has not been established. Moreover, in vivo usage of such a cofactor by any class Ic RNR remains to be demonstrated.

Since its discovery, the structure of the novel heterodinuclear cofactor of *Ct* RNR and its mechanism of assembly have been extensively studied.^{12, 13, 15, 17-20} It was shown that apo α_2 can assemble the active cofactor from the divalent metals and O_2 via a $\text{Mn}^{\text{IV}}/\text{Fe}^{\text{IV}}$ intermediate.¹³ An electron shuttled to the cluster (via neighboring Tyr 222 and Trp 51) reduces the Fe^{IV} site of the intermediate to form the stable and active $\text{Mn}^{\text{IV}}/\text{Fe}^{\text{III}}$ state.¹⁴ Two separate X-ray crystallographic studies showed that forms of α_2 having Mn in site 1 (this cofactor form is hereafter denoted $\text{Mn}^{\text{IV}}/\text{Fe}^{\text{III}}$) predominate upon assembly of the cofactor either in vitro²¹ or during heterologous expression in *E. coli*.²² Additionally, the former study revealed some Mn occupancy in site 2 under certain metal loading conditions, suggesting production of lesser amounts of the $\text{Fe}^{\text{III}}/\text{Mn}^{\text{IV}}$ complex.²¹ A negative correlation between the prevalence of this complex in different preparations and their catalytic activities implied that the form of the protein with Mn in site 2 is less active or inactive (Figure 2).

The steps of the cofactor assembly reaction preceding the $\text{Mn}^{\text{IV}}/\text{Fe}^{\text{IV}}$ intermediate remain poorly understood. For example, almost nothing is known about how the two different divalent metal ions selectively occupy their functional sites, nor is the mode of addition of O_2 to the $\text{Mn}^{\text{II}}/\text{Fe}^{\text{II}}$ (or $\text{Fe}^{\text{II}}/\text{Mn}^{\text{II}}$) state known. In previous work, two different reconstitution procedures yielded different distributions of the more active $\text{Mn}^{\text{IV}}/\text{Fe}^{\text{III}}$ and less active (or inactive) $\text{Fe}^{\text{III}}/\text{Mn}^{\text{IV}}$ forms.²¹ In the first procedure (procedure 1), apo α_2 was pre-loaded with 1.5 equivalents (equiv) Mn^{II} per α monomer, (slightly greater than the experimentally determined stoichiometry of functional sites) in the presence of ambient O_2 , and Fe^{II} was then added very slowly to a final 0.75 equiv per monomer. The underlying rationale was to use the anticipated lability of Mn^{II} in the site designed to bind Fe^{II} to direct Fe^{II} incorporation into this site, with rapid addition of O_2 irreversibly trapping a single cluster form. This procedure yielded Mn occupancy primarily of site 1 but with significant additional occupancy of site 2. In the second procedure (procedure 2), the quantity of Mn^{II}

initially added was diminished to less than the experimental stoichiometry of functional sites and varied systematically. Fe^{II} was then injected rapidly in the presence of ambient O₂. Procedure 2 resulted in diminished Mn occupancy of site 2 and greater catalytic activity on a per Mn basis. However, catalytically inactive Fe₂^{III/III} clusters predominated at the lowest initial Mn^{II}/ ratios. Permitting the Mn/Fe cofactor to assemble during overexpression of *Ct*₂ in *E. coli* with Mn^{II} supplementation resulted in an outcome similar to that of in vitro assembly procedure 2.²² The propensity of the *Ct*₂ protein to assemble multiple cluster forms in addition to the (more) active configuration motivated further exploration of the structural and dynamic bases for the selective assembly of the most active state.

For the class Ia and Ib RNRs, comparison of the X-ray crystal structures of the apo *Ct*₂ proteins,^{23, 24} their Mn₂^{II/II} and/or Fe₂^{II/II} complexes,²⁵⁻²⁹ and the corresponding oxidized states^{7, 8, 28, 30} revealed the structural adjustments that accompany metallocofactor assembly and activation. Expanding the comparison to include published structures of oxidized *Ct*₂ shows that, although orthologs of each subclass are distinguished from the members of the other two by the combination of metal ions utilized in the active cofactor, the structures of the oxidized metallocofactors remain remarkably similar across all three subclasses.² In each case, the site comprises two His and four carboxylate (Glu or Asp) ligands arranged similarly around the metal subsites. This structural similarity has been cited as a rationale for improper incorporation of Mn^{II} into class Ia *Ct*₂ proteins and Fe^{II} into class Ib and Ic *Ct*₂s.³¹ Nevertheless, analysis of the class Ia Fe₂^{II/II}-*Ct*₂ and class Ib Mn₂^{II/II}-*Ct*₂ structures shows that the surrounding protein scaffold provides distinct coordination environments for Mn^{II} or Fe^{II} (Figure 1A-E), channels tailored to transport a specific oxidant (O₂ or O₂⁻) to the metal binding site, and, in the class Ib system, a distinct interaction surface for binding of an accessory protein.²⁵⁻²⁷

In this work, we investigate whether the class Ic *Ct*₂ subunit might possess specific adaptations (to its metal sites or the surrounding protein) first to promote assembly of the proper (Mn^{II}/Fe^{II}) reduced precursor to the functional cofactor and then to direct its reaction with O₂ to generate the active Mn^{IV}/Fe^{III} state. Structures of the apo and Mn^{II}/Fe^{II} complexes were determined by X-ray crystallography; the latter complex was prepared by co-crystallization of *Ct*₂ in the presence of stoichiometric Mn^{II} and Fe^{II} under anoxic conditions. These structures show that the Mn^{II}/Fe^{II} state (with Mn in site 1, as previously concluded)^{21, 22} assembles efficiently with only low levels of incorrect cluster configurations (Fe^{II}/Mn^{II}, Mn₂^{II/II}, or Fe₂^{II/II}) (Figure 2). The structures thus imply that the metal-binding site has sufficient inherent selectivity to direct Mn^{II} to site 1 and Fe^{II} to site 2 as long as the metals are provided in proper stoichiometry and metal incorporation is controlled by thermodynamics (i.e., by allowing sufficient time for equilibration of the metals with the protein prior to addition of O₂) rather than kinetics. Indeed, preparations reconstituted in this manner were found by EPR analysis to be more homogeneous than those produced in the previous studies and by activity assays to be the most active preparations characterized to date. Intriguingly, diffraction data on crystals prepared from solutions of the apo protein and with Mn^{II} only reveal Mn occupancy of both metal sites, although not necessarily simultaneously, even with sub-stoichiometric quantities of Mn^{II}, suggesting that the selective assembly of the Mn^{II}/Fe^{II} reactant state might arise from the preference of Fe^{II} for site 2. Neither the surprisingly high degree of site-selectivity in metal binding nor the efficient reaction of the resultant Mn^{II}/Fe^{II} complex with O₂ appears to be coupled to protein dynamics, as the dispositions of the metal ligands in the apo and Mn^{II}/Fe^{II} metallated forms are virtually identical, and only minor adjustments (displacement of a water and rearrangement of a single carboxylate residue) are seen upon oxidation of the cluster. Comparison of the structures of the reduced and oxidized forms suggests that Fe^{II} is poised to add O₂ in a side-on fashion during activation of the cofactor, leading to subsequent coupling to the Mn ion concomitant with cleavage of the O–O bond.

EXPERIMENTAL PROCEDURES

Overexpression and purification of apo Ct β_2

The construction of the plasmid containing the gene (*nrdB*) that encodes Ct β_2 has been described.¹² This construct expresses the protein with an N-terminal His₆ affinity tag comprising 20 total additional residues. Procedures for purification of the protein in its apo form have been described previously.¹²

General crystallographic methods

All crystallographic datasets were collected at the Life Sciences Collaborative Access Team (LS-CAT) and the General Medical Sciences and National Cancer Institutes Structural Biology Facility (GM/CA-CAT) beamlines at the Advanced Photon Source. Datasets were indexed, integrated, and scaled with the HKL2000 software package.³² All structures were solved by molecular replacement using PHASER³³ with the structure of an Fe^{III/III}₂-monomer (PDB accession code 1SYU) as the search model. The resulting initial models were used as the basis for further refinement and model building with Refmac5³⁴ and Coot³⁵, respectively. Tables S1-S8 report all data collection and refinement statistics. Figures were generated with the PyMOL Molecular Graphics System.³⁶ Structural superpositions were performed using the secondary-structure matching (SSM) alignment method.³⁷ Electron density maps were calculated with FFT.³⁸ Fe-specific maps were generated using a subtraction procedure³⁹ with FFT and SFTOOLS.

Determination of the X-ray crystal structure of apo β_2

Crystals of apo β_2 were grown from solutions of 10-30 mg/mL protein in 20 mM HEPES, pH 7.6, 5-10% glycerol using the hanging drop vapor diffusion method at room temperature with 100 mM HEPES, pH 7.5, 200 mM sodium acetate, 10% (w/v) PEG 3000 as the precipitant. Colorless crystals appeared within two weeks and were overlaid with cryoprotectant solution [well solution supplemented with 50% (v/v) glycerol], mounted on rayon loops, and flash-frozen in liquid nitrogen for data collection. Data collection and refinement statistics are reported in Table S1.

The asymmetric unit (ASU) consists of four monomers arranged into two β_2 dimers. As observed previously,²¹ the N-terminal affinity tag mediates an intermolecular interaction between adjacent β_2 dimers in three of the four molecules in the ASU. The final model includes residues 1-322 for chain A (with nine additional residues from the affinity tag), residues 1-328 for chain B (with eight additional tag residues), 1-329 for chain C (with two additional tag residues), residues 1-328 for chain D (with six additional tag residues), and 888 water molecules. Ramachandran plots generated with Molprobity⁴⁰ indicate 99.5% of residues in favorable regions and 100% of residues in the allowed and generously allowed regions.

Determination of the X-ray crystal structure of Mn^{II}/Fe^{II}- β_2

Apo β_2 was loaded with one equiv (per monomer) MnCl₂ (10 mM solution in 50 mM HEPES, pH 7.5) and degassed via 5 cycles of vacuum purge followed by refilling with Ar on a Schlenk line. All subsequent manipulations were carried out with stringently degassed solutions of crystallization and cryoprotection reagents in a Coy anaerobic chamber with an atmosphere of 5% H₂/95% N₂. One equiv (per monomer) (NH₄)₂Fe(SO₄)₂ (10 mM solution in 50 mM HEPES, pH 7.5) was added to the degassed protein solution. Crystals of the metal-loaded protein were grown by hanging drop vapor diffusion at room temperature with 100 mM HEPES, pH 7.2, 200 mM sodium acetate, 10% (w/v) PEG 3000 as the precipitant. Colorless or very light green crystals appeared within two weeks. Crystals were prepared for data collection by covering the crystal drop with cryoprotectant solution [well

solution supplemented with 50% (v/v) PEG 400], mounting on rayon loops, and flash-freezing in liquid nitrogen. Data collection and refinement statistics are reported in Table S2.

The asymmetric unit (ASU) consists of four monomers with the same arrangement as described for crystals of apo β_2 . The final model includes residues 1-327 for chain A (with six additional residues from the affinity tag), residues 1-320 for chain B (with nine additional tag residues), 1-327 for chain C (with six additional tag residues), residues 1-328 for chain D (with two additional tag residues), four Mn^{II} ions, four Fe^{II} ions, one acetate molecule, one PEG 400 molecule, and 1027 water molecules. Ramachandran plots generated with Molprobity⁴⁰ show 99.4% of residues in favorable regions and 100% of residues in the allowed and generously allowed regions. Metal ion occupancies were independently refined with PHENIX.⁴¹ Tables 1 and S9 show anomalous map peak heights for each metal binding site.

Tables S3-S4 and S7-S8 present crystallization conditions and data collection statistics for crystals of the protein grown with Mn^{II} only (at 1 or 2 equiv per β_2), Fe^{II} only, or 1 equiv of each metal. Mn^{II}-only samples were crystallized outside of the anaerobic chamber as described for the apo protein. Fe^{II}-containing samples were loaded with metal and then crystallized in the anaerobic chamber, as described for the Mn^{II}/Fe^{II}- β_2 crystals. These samples were later exposed to O₂ during crystallization or crystal harvest.

Preparation of Mn^{IV}/Fe^{III}- β_2 for activity measurements

As summarized in Table 2, different ratios of Mn^{II} and Fe^{II} were premixed in an anoxic chamber and added to an O₂-free solution of apo β_2 . After a brief incubation (5-10 min), a solution of O₂-saturated (at 5 °C) reaction buffer (100 mM HEPES, 10% v/v glycerol, pH 7.6 at 4 °C) was added to the Mn^{II}/Fe^{II}- β_2 solution. Excess and/or weakly bound metals were removed as previously described.^{20, 21} The quantity of each metal retained was determined by inductively coupled plasma atomic emission spectroscopy (ICP-AES).

Crystallization of Mn^{IV}/Fe^{III}- β_2

Crystals of the Mn^{IV}/Fe^{III} form of β_2 were obtained from 10-30 mg/mL protein solutions prepared in 20 mM HEPES, pH 7.6, 5-10% glycerol. The Mn^{IV}/Fe^{III} form was generated from the apo protein by the reconstitution procedure described above and crystals were grown using the hanging drop vapor diffusion method at room temperature with either 100 mM HEPES pH 7.0, 200 mM sodium acetate, 5% (w/v) PEG 3000 or 100 mM HEPES pH 7.2, 200 mM sodium acetate, 5% (w/v) PEG 3000 as the precipitant. Pale yellow crystals appeared within two weeks and were overlaid with cryoprotectant solution (precipitant solution supplemented with 50% (v/v) PEG 400), mounted on rayon loops, and flash-frozen in liquid nitrogen for data collection. Data collection statistics are provided in Tables S5 and S6.

RESULTS

X-ray crystal structure of apo β_2

The crystal structure of apo β_2 (Table S1) was determined to a resolution of 1.7 Å and contains four monomers arranged into two β_2 dimers. Together these afford four independent views of the metal binding site prior to initiation of metallocofactor assembly. The apo protein adopts an overall fold that is nearly identical to that in metal loaded forms of the protein (Figure S1) (0.46 Å rmsd for 317 C atoms in a single monomer). Electron density maps of the site (Figure S2) show that the ligands are generally well-ordered despite the absence of metal ions. Anomalous scattering datasets collected at the Mn and Fe X-ray absorption *K*-edges (Table S1) yielded difference maps confirming the absence of these

metal ions from the cofactor site and elsewhere in the structure (Figure S2). Additionally, significant electron density for ordered solvent is not observed at the cofactor site, although in some views, weak positive difference density that could potentially arise from disordered water molecules was observed.

The metal-coordinating residues (Figure 1F) cluster together within hydrogen-bonding distance of one another. Such close clustering of ligands indicates protonation of some of the Asp/Glu/His metal-binding residues, as proposed for the class Ia and Ib apo β_2 proteins.^{23, 24} In the structure of the *Ct* class Ic apo β_2 protein, the metal binding residues near metal site 2 (Glu 227, Glu 193, and His 230) associate particularly tightly (Figure 1F), further highlighting that some of them are protonated (Figure S3). Near site 1, *Ct* β_2 differs from the class Ia and Ib proteins in its substitution of a Glu for an Asp in the coordination sphere and a Phe for a Tyr in the second sphere at position 127 (*Ct* β_2 numbering).⁴² In the class Ia and Ib apo β_2 structures,^{23, 24} the shorter Asp side chain and Tyr residue in the second sphere interact with each other and result in a more open configuration at site 1. In class Ic β_2 , the larger Glu side chain at position 89 allows the residue to hydrogen bond with both the other site 1 ligand His 123 and the bridging residue Glu 120. This interaction suggests that both His 123 and Glu 120 might be protonated (Figure S3). The Tyr to Phe substitution removes a competing hydrogen bond in the second sphere, permitting Glu 120 to engage in closer and more numerous interactions with the other site 1 ligands. The Phe 127 substitution, in combination with the position of surrounding hydrophobic residues (Figure S4), further encourages close packing of the ligands near site 1.

Whereas the ligands associated with each individual site interact strongly with one another in the apo protein, very little hydrogen bonding is observed between sites (Figure S3). Only one potential interaction is possible, between Glu 120 and Glu 193, but the orientation is suboptimal and the hydrogen bonding capacity of Glu 193 is fully saturated by its interactions with Glu 227 and His 230. The position of hydrophobic residue Phe 197 further defines a steric barrier between sites (Figure S4). Interestingly, the orientation of this residue does not change upon metal loading (vide infra), in contrast to what is observed in other class I β_2 structures (Figure 1A-D). The lack of hydrogen bonds and the presence of a steric barrier between the sites may limit cooperative metal binding in this system, important for assembly of a heterobimetallic center.

X-ray crystal structure of Mn^{II}/Fe^{II}- β_2

An X-ray crystal structure of the reduced Mn^{II}/Fe^{II} form of the protein was determined to a resolution of 1.80 Å and obtained by loading apo protein with one equiv each (per monomer) of Mn^{II} and Fe^{II} (two equiv total) and crystallizing the resulting metal-loaded protein anaerobically (Table S2). Diffraction data were collected at the Mn and Fe X-ray absorption *K*-edges to calculate Mn- and Fe-specific anomalous difference maps (Figure 3A) and assign metal site occupancies. Since Mn contributes significantly to the X-ray absorption at the Fe *K*-edge, the Fe-specific difference map was generated by a subtraction procedure³⁹ to eliminate the contribution from Mn. These maps indicate that Mn^{II} binds in site 1 and Fe^{II} in site 2. Importantly, this result provides further evidence that the (more) active cofactor configuration contains Mn^{IV} in site 1 and Fe^{III} in site 2, as suggested by previous crystallographic characterization of the oxidized form.^{21, 22} However, in this new structure, the metals ions appear to have partitioned into their functional sites with greater selectivity. In all four views of the metal binding site, Mn anomalous density at site 2 is below the background level (5.0-6.0 σ)⁴³ (Table 1), and no anomalous density for Fe is seen at site 1 (Table S9).⁴⁴ The most obvious difference in the metal loading strategy employed here is the provision of both metals in a 1:1 stoichiometry per monomer prior to any exposure to O₂. This procedure should, in contrast to those used in the previous studies, permit the Mn^{II} and Fe^{II} ions to reach equilibrium within the metal binding site over a

period of days while crystallization occurs. In other words, metal binding should, in this case, be solely under thermodynamic control. Excitingly, this result suggests that the protein scaffold provides an intrinsic basis to localize Mn^{II} to site 1 and Fe^{II} to site 2, even with the more labile divalent metal ions.

Our successful crystallization of *Ct*₂ with bound Fe^{II} is somewhat surprising because, to date, no crystal structure of a class I₂ protein has been solved with Fe^{II} introduced during crystallization. The difficulty in crystallizing Fe^{II/II}₂ forms of the protein is believed to result from the dynamic nature of the interaction between Fe^{II} and the₂ metal binding sites. Fe^{II/II}₂-₂ structures have instead been determined by soaking apo protein crystals with Fe^{II} ions^{25, 27} or by chemical or photoreduction of crystals of Fe^{III/III}₂-₂.^{28, 29} The former approach, soaking metal ions into apo protein, has yielded structures differing from those obtained after reduction of Fe^{III/III}₂-₂. The structures obtained by Fe^{II} soaks are more consistent with CD and MCD characterization of the Fe^{II/II}₂ state⁴⁵ and thus provide a more appropriate starting point for analysis of the O₂ reaction. The co-crystallization approach used here for *Ct* Mn^{II}/Fe^{II}-₂ should similarly afford the appropriate O₂-reactive state. It is possible that the presence of Fe^{II} in a heterobimetallic cluster with Mn^{II} or specific properties of the cofactor site in *Ct*₂ promote more stable Fe^{II} binding. An alternative scenario is that, even though the protein was crystallized and prepared for X-ray data collection in a stringently anaerobic environment, the sample became oxidized by trace O₂ and subsequently crystallized as the oxidized form. Several observations provide argument against this possibility. The long Mn-Fe separation of 3.2 Å (compared to the 2.9 Å determined by EXAFS spectroscopy for the Mn^{IV}/Fe^{III} state) and the long 2.1-2.3 Å bonds between the Mn and Fe ions and the bridging water ligand (Figure 4) are more consistent with a lower oxidation state of the cluster (e.g., Mn^{II}/Fe^{II}). Although these structural features could potentially have arisen from photoreduction of oxidized Mn/Fe centers during data collection at 100 K,⁴⁶ the observed μ^{-1, 2} binding mode of Glu 227 (Figures 1G, 4, S5, and S6), also consistent with a reduced cofactor, is less likely to have arisen by cluster photoreduction and a accompanying carboxylate shift. We therefore conclude that the structure represents the Mn^{II}/Fe^{II} state and not a more oxidized form.

The resolution (1.8 Å) and homogeneous configuration of the Mn^{II}/Fe^{II} cofactor in this structure provide a basis to begin to understand how the protein controls site selectivity during metal uptake and reaction with O₂ to form the active cofactor. The diffraction data were used to generate a fully refined model (Table S2), in which the Mn^{II} and Fe^{II} ions at each metal-binding site can be modeled at full or nearly full occupancy and the ligands are generally well ordered (Figure S5).⁴⁷ The first coordination sphere (Figure 1G) shares many features in common with those seen in other structures of reduced class Ia and Ib₂ proteins (Figure 1B, 1D, 1E).²⁵⁻²⁷ Each metal ion is coordinated by a histidine and three carboxylate side chains, of which two (Glu 98 and Glu 227) bridge the metal ions. All metal-ligand bond distances fall within the range of 1.9-2.3 Å (Figure 4), similar to other Fe^{II}-O/N or Mn^{II}-O/N distances observed in class Ia and Ib₂ crystal structures. The μ^{-1, 2} coordination mode of Glu 227 found here is identical to that observed in other structures, obtained by soaking or cocrystallization methods, of reduced class I Mn₂^{II/II}- and Fe₂^{II/II}-₂ proteins.^{25, 27} This chelating/bridging mode is distinct from the monodentate position adopted by the residue in structures of the corresponding oxidized complexes (Figure S6).

Mn^{II}-occupied site 1 is six-coordinate with two exogenous solvent-derived molecules (modeled as waters w1 and w2) completing the first coordination sphere (Figures 1G, 4). High coordination numbers and the presence of bound water ligands have been observed in the structures of other Mn^{II}-substituted class Ia and Ib₂ proteins (Figure 1D, 1E).^{25, 26, 48} Interestingly, the class Ic Mn^{II}/Fe^{II}-₂ structure shows significant distortion along the Mn^{II}-

w2 axis (Figure 5), enforced by the position of Phe 197 in the outer sphere (Figures 1, S4) and by the sharing of the w2 ligand with Fe^{II} in site 2 (Figures 1G, 5).

The configuration of Fe^{II} in site 2 is also distinct from those in the structures of Fe^{II}-substituted forms of other class I β_2 proteins. As for Mn^{II} in site 1, Fe^{II} is six-coordinate with a bound water ligand. In other class Ia and Ib β_2 structures, Fe^{II} exhibits highly distorted 4- or 5-coordinate geometries, and solvent waters are typically absent from the first coordination sphere (Figures 1B, S6).^{25, 27, 45} The site 2 configuration in the Mn^{II}/Fe^{II} complex of Ct β_2 is also geometrically distorted along the Fe^{II}-w2 axis, for the same reasons cited above for site 1. More subtle distortion in the plane defined by the Glu ligands is also evident and arises from the chelation mode of Glu 227 and the tightly constrained position of Glu 193, which results in a short (1.9 Å) Fe^{II}-O bond.

Comparison of the ligand positions in the apo and Mn^{II}/Fe^{II} forms of Ct β_2 (Figure 1F, 1G) reveals little change between the two, suggesting minimal net movement during metal uptake. The only significant ligand conformational change is a slight rotation of the Glu 120 carboxylate resulting in a *syn-syn* μ -1,3 bridging configuration. This coordination mode is also seen in the structures of class Ib β_2 proteins with Mn^{II} but differs from those in the Fe^{II}-substituted class Ia and Ib proteins, where it is either *syn-anti* or *anti-syn*.²⁵⁻²⁷ The *syn-syn* mode may better accommodate the higher coordination numbers and octahedral geometry observed in other Mn^{II} β_2 structures (Figure 5) and in the Mn^{II}/Fe^{II}- β_2 complex described here.

The Mn^{II}-Fe^{II} separation indicated by the crystallographic data is 3.2 Å. This value is unexpectedly short, especially when it is compared with the corresponding distances seen in other crystal structures: Mn^{II}-Mn^{II} and Fe^{II}-Fe^{II} distances have ranged from 3.5 to 4.0 Å.^{25-27, 48} Indeed, even within the same protein scaffold (Ct β_2), the inter-metal distance expands to 3.5 Å in the Mn^{II} β_2 complex (vide infra), suggesting that only the fully-occupied heterobimetallic state exhibits the close approximation of the metal ions in the reduced cluster form. Recent X-ray absorption spectroscopic characterization reported a Mn-Fe separation of 3.5-3.65 Å in forms of the enzyme generated by chemical reduction or following prolonged exposure to X-ray radiation (presumably generating primarily Mn^{II}/Fe^{II} clusters).⁴⁶ However, the lack of identification and quantification of all cluster forms present in these samples renders interpretation of the results perilous. The 3.2 Å Mn-Fe distance observed here is comparable to the Fe^{II}-Fe^{II} distance (3.3 Å) found in a crystal structure of the reduced (Fe^{II}) β_2 form of soluble methane monooxygenase hydroxylase (sMMOH),⁴⁹ a distantly related member of the large family of ferritin-like dimetal-carboxylate proteins.^{50, 51} Interestingly, the two defining substitutions that distinguish the class Ic Ct β_2 protein from the class Ia and Ib orthologs (Glu 89 in place of Asp in metal site 1 and Phe 127 at the position corresponding to the radical tyrosine) are also preserved in sMMOH as a Glu and Cys, respectively. The comparison suggests that the larger carboxylate ligand at site 1 and outer sphere interactions may favor a closer approach of the divalent metals. In terms of function, the close proximity of the metal centers in the Mn^{II}/Fe^{II} complex of Ct β_2 could have important implications for the mechanism of the activation reaction, especially the mode of initial addition of O₂ to the reduced cluster.

Crystallographic analysis of Mn^{II}- β_2

X-ray diffraction datasets collected on crystals of Ct β_2 grown from protein loaded with Mn^{II} only (Figure S7, Tables S3 and S4) reveal partial metal occupancy of both site 1 and site 2. The observed occupancies could result from Mn^{II} binding to site 1 in 50% of the monomers and to site 2 in the other 50%. Alternatively, it could also be the outcome of highly cooperative Mn^{II} binding to form a fully occupied Mn^{II} β_2 cluster in half of the monomers and an unoccupied apo site in the other half. We also attempted X-ray diffraction

experiments on crystals exposed (during cocrystallization or in crystal soaking experiments) to Mn^{II} in excess of the number of binding sites in an effort to achieve a fully occupied $\text{Mn}^{\text{II/III}}_2$ center in both subunits. These efforts yielded, at maximum, 90% occupancy of site 2 and 70% occupancy of site 1 (metal ion occupancies determined by refinement⁴¹ and visual inspection of the $F_o - F_c$ difference map). The metal-metal distance is 3.5 Å in these structures and two waters are present at positions similar to those in the $\text{Mn}^{\text{II/III}}/\text{Fe}^{\text{II}}$ structure, but the $\text{Mn}^{\text{II}}\text{-OH}_2$ distances are much longer (2.3-2.4 Å). These structures highlight the difficulty in forming a fully-occupied $\text{Mn}_2^{\text{II/III}}$ cluster in this protein and show that Mn^{II} does not localize solely to site 1 in the absence of Fe^{II} . Additionally, loading of Mn^{II} does not induce significant conformational changes in the metal binding site.

Reconstitution of active $\text{Mn}^{\text{IV}}/\text{Fe}^{\text{III}}\text{-}\beta_2$ and crystallographic confirmation of metal-site selectivity

The $\text{Mn}^{\text{II}}/\text{Fe}^{\text{II}}\text{-}_2$ complex implies that Mn^{II} binds only in site 1 and Fe^{II} only in site 2 when the divalent metal ions are provided in the proper proportions and allowed to reach equilibrium in the absence of O_2 (i.e., controlled by the binding thermodynamics rather than kinetics, as in previous studies). This finding suggested that reconstituting the protein in this manner might afford homogeneous and maximally active preparations. To test this prediction, samples activated by three different procedures, each starting with a different $\text{Mn}^{\text{II}}:\text{Fe}^{\text{II}}$ ratio (Table 2, procedures 3A-3C), were evaluated. In procedure 3A, Mn^{II} was added at 2 equiv and Fe^{II} at 0.65 equiv per monomer. In procedure 3B, Mn^{II} and Fe^{II} were added in equal quantities, each at 1 equiv per . In procedure 3C, Fe^{II} was added at 2 equiv and Mn^{II} at 0.65 equiv per . In each case, the cofactor was assembled by allowing the divalent metal ions to bind and reach equilibrium prior to addition of O_2 . Following removal of unincorporated metal ions by dialyzing the protein against EDTA-supplemented buffer (excess EDTA was removed by further dialysis against buffer lacking EDTA), the resultant $\text{Mn}^{\text{IV}}/\text{Fe}^{\text{III}}\text{-}_2$ complexes were analyzed by ICP-AES (metal quantification), X-ray crystallography, EPR spectroscopy, and RNR activity assays. Although the quantity of total metal added to $_2$ was sufficient to support full occupancy, ICP-AES analysis revealed that the protein retained ~ 50% of the total metal added (Table 2). This result is consistent with previous observations that the stoichiometry of functional metal sites is less than the theoretical complement.^{21, 52} The ratio of Mn:Fe retained was roughly 1:1 in the procedure-3A and procedure-3B samples, whereas the procedure-3C sample, not surprisingly, retained significantly more Fe than Mn. The ability of these preparations of $\text{Mn}^{\text{IV}}/\text{Fe}^{\text{III}}\text{-}_2$ to support ribonucleotide reduction was assessed using the published LC-MS assay.¹⁴ The preparations were found to possess the greatest catalytic activity per monomer (Table 2) yet reported.²¹ On a per Mn basis, the activities are comparable to those of samples from the previous study that were shown by X-ray crystallography to contain Mn primarily at site 1.²¹ After reduction of the $\text{Mn}^{\text{IV}}/\text{Fe}^{\text{III}}\text{-}$ complexes to the EPR-active $\text{Mn}^{\text{III}}/\text{Fe}^{\text{III}}$ state by treatment with dithionite, X-band EPR spectra were acquired (Figure S8). The spectra are similar to those previously assigned to $\text{Mn}^{\text{III}}/\text{Fe}^{\text{III}}\text{-}_2$ complexes with Mn^{III} almost exclusively in site 1 (procedure 2) and different from those arising from samples with a potentially more heterogeneous distribution of $\text{Mn}^{\text{III}}/\text{Fe}^{\text{III}}$ and $\text{Fe}^{\text{III}}/\text{Mn}^{\text{III}}$ clusters (procedure 1).²¹ These results indicate that the new reconstitution procedure (relying on the thermodynamic control of Mn^{II} and Fe^{II} binding to apo protein) yields more selective incorporation of Mn at site 1, generating preparations with greater catalytic activity than previously reported.

Crystals were grown from the samples reconstituted to the active state by procedure 3A and procedure 3B. X-ray diffraction data were collected (Tables S5, S6) at wavelengths appropriate to calculate Mn- and Fe-specific anomalous difference maps (Figure 3B) and locate the metals in the active site. In each case, the crystals contain four monomers per

ASU, offering four independent views of the metal binding site. In all eight views, the Mn anomalous scattering peaks dominate in site 1 (Table 1) and the peak heights in site 2 are well below the background level (defined as 5.0-6.0). The anomalous scattering data demonstrate that Mn partitions cleanly into site 1 and Fe into site 2 in these samples, as found in the structure of the Mn^{II}/Fe^{II}-₂ complex.

The structural features of the cofactor site are generally consistent with those found in the published structures of protein crystallized as the Fe^{III/III}₂ and Mn^{IV}/Fe^{III} complexes of *Ct*₂.^{21, 42} The electron density maps suggest that Glu 227 moves from a μ -^{1, 2} bridging position to a monodentate coordination mode at site 2 during the activation reaction (Figure S6), consistent with analogous carboxylate shifts that have been proposed in other class I ₂ proteins.⁵² In addition, two new (non-protein) bridging oxygen ligands, which could presumably originate from O₂ as it is reduced to the oxidation state of water during the reaction, are evident in the oxidized complex. However, the modest resolution (1.90-2.20 Å) and low overall metal occupancy (< 50%) limit our ability to elicit additional structural details for the oxidized cluster. The active metallocofactor is susceptible to X-ray-induced photoreduction,^{20, 46} as is generally a major challenge in accurate structural characterization of high-valent metalloenzyme intermediates by X-ray crystallography.⁵³ The effects of X-ray photoreduction during cryocrystallography, with the sample maintained at 100 K during data collection, are probably limited to slight elongation of metal-ligand bonds and metal-metal distances rather than large-scale ligand movements and dissociations. Thus, the conformational change of Glu 227 and introduction of new bridging oxygen ligands observed in the structure of the oxidized complex^{21, 42} (Figure S6) are very likely to be authentic structural changes associated with activation. A complete picture of the structure of the active metallocofactor will require corroborating data from an ensemble of methods as well as a still-absent high-resolution X-ray crystal structure of *Ct*₂ with a fully occupied and homogeneous Mn^{IV}/Fe^{III} cluster.

DISCUSSION

Structural basis for metal ion site selectivity

A comparison of the coordination environment in the Mn^{II}/Fe^{II} complex of *Ct*₂ to those in the homodinuclear (Fe^{II/II}₂ or Mn^{II/II}₂) complexes of the class Ia or Ib ₂ proteins provides a rationale for how the structure of the class Ic ₂ protein might direct Mn^{II} to site 1 and Fe^{II} to site 2. The most relevant comparisons for understanding the occupancy of site 1 by Mn^{II} are to the structures of the class Ib Mn₂^{II/II}-_{2s},^{25, 26} proteins in which the Mn^{II/II}₂ state is the relevant starting point for cofactor activation^{8-10, 54} and the cofactor site is therefore expected to be optimized for Mn^{II} selectivity. In these structures, the Mn^{II} centers are 5- or 6-coordinate and include exogenous solvent ligands in the primary coordination sphere (Figures 1, 5). As observed previously,^{25, 26} the geometry trends towards an ideal octahedron, a configuration typical of a high-spin Mn^{II} *d*⁵ electronic configuration.⁵⁵ High-affinity Mn^{II} binding sites in other proteins such as calprotectin^{56, 57} and Mn catalase⁵⁸ are also commonly six-coordinate with octahedral geometry. In the *Ct* Mn^{II}/Fe^{II}-₂ structure, both metal sites are six-coordinate and have exogenous solvent ligands, but severe distortion exists at each site along the w2 axis, enforced by the position of a Phe residue between the two sites (Figure 1, Figure SD1). The position and bulky nature of the Phe side chain makes it impossible for the water to bind solely to the Mn^{II} ion in site 1 or for each metal to coordinate an axial water. The distortion at site 2 is perhaps made even more pronounced by the chelating mode of Glu 227 at site 2 and the short metal-ligand bond with Glu 193 (Figure 5). These binding modes are driven by a hydrogen-bonding network in the secondary sphere (Figure S4) that forces Glu 193 into a tight monodentate bond with the site 2 metal, opening a coordination position that is filled by the chelating interaction with Glu 227 at this site. The six-coordinate environment and the ability to accommodate waters in

the first coordination sphere may favor occupancy by Mn^{II} at both sites, but it is not obvious that site 1 should be more stringent than site 2 in selectivity for Mn^{II} over Fe^{II} . An alternative proposal is that the geometric distortion, particularly at site 2, could favor Fe^{II} binding by stabilizing the asymmetrically filled t_{2g} shells of a high-spin d^6 electronic configuration in a weak octahedral ligand field.⁵⁵ Distortions of this type in Fe^{II} complexes have been predicted computationally⁵⁹ and the observation that other class I O_2 structures with Fe^{II} exhibit lower coordination numbers and distorted geometries^{25, 27} lends further support to this mechanism for enforcing Fe^{II} selectivity at site 2.

The seemingly rigid nature of the metal binding sites in Ct_{O_2} and the influence of the surrounding protein in defining the coordination geometry is reminiscent of the entatic-state model for metal-protein interactions.⁶⁰ Here, the metal binding site of Ct_{O_2} could perhaps be viewed as an entatic state designed to select between two different metals with subtly different coordination preferences. The geometry of the Ct_{O_2} metal binding sites imposes a sufficiently unfavorable environment for Mn^{II} interaction that Fe^{II} is allowed to displace it, particularly in site 2. This strategy would lead to selective formation of the $\text{Mn}^{\text{II}}/\text{Fe}^{\text{II}}$ cluster when Mn^{II} is in excess and Fe^{II} is limiting. Additional experimental analysis will be necessary to validate this model for class Ic metallocofactor assembly. The rigid nature of much of the class Ic O_2 ligand framework after metal binding is also likely to be important in the O_2 reaction to activate the cofactor and in control of the reversible RT that initiates and terminates nucleotide reduction.

The observation from the class Ic O_2 structures that the ligands remain in largely the same position in the presence and absence of the metal ions stands in stark contrast to the situations in the class Ia and Ib proteins.^{23, 24} In comparison to their apo proteins, the metal-bound forms (Figure 1) in these systems show changes in the conformations and/or positions of several ligands, particularly the residues cognate to Ct_{O_2} Glu 193.²⁵⁻²⁷ Conformational changes of side chains during metal binding in class Ia or Ib O_2 proteins could encourage cooperative binding to favor efficient assembly of the appropriate homodinuclear metallocofactor precursor. Conversely, the near complete absence of ligand movement upon metal binding to the class Ic O_2 could be part of an adaptation to inhibit formation of $\text{Mn}^{\text{II/II}}_2$ or $\text{Fe}^{\text{II/II}}_2$ centers that would ultimately lead to an inactive cofactor.

Structural insight into oxidative activation of the cofactor by O_2

The next step in metallocofactor assembly in Ct_{O_2} is reaction of the $\text{Mn}^{\text{II}}/\text{Fe}^{\text{II}}$ center with O_2 to form the $\text{Mn}^{\text{IV}}/\text{Fe}^{\text{IV}}$ intermediate,¹³ which, upon one-electron reduction of the Fe^{IV} site, is converted to the stable and active $\text{Mn}^{\text{IV}}/\text{Fe}^{\text{III}}$ state.^{12, 17} The location and mode of O_2 addition and the protein structural changes that accompany the reaction are not known. O_2 is likely to interact first with Fe^{II} , which has the more appropriate oxidation potential to reduce O_2 .⁶¹ With firm evidence now in hand that Fe^{II} is located at site 2, the proposal that O_2 adds to Fe^{II} aligns with studies on the class Ia Ec_{O_2} oxygen binding site⁶² and analysis of crystal structures of the reactant ($\text{Mn}^{\text{II/II}}_2$) forms of class Ib O_2 ,^{25, 26} which all suggested that the oxidant (O_2 or $\text{O}_2^{\bullet-}$) adds first to the site 2 metal.

Comparison of the structure of the oxidized form of the class Ic O_2 to that of the reduced ($\text{Mn}^{\text{II}}/\text{Fe}^{\text{II}}$) form reveals additional clues to how O_2 might interact with the Fe^{II} center. The cofactor of the $\text{Mn}^{\text{II}}/\text{Fe}^{\text{II}}$ - O_2 complex lacks open coordination sites, suggesting that O_2 must displace existing ligands. The most likely candidates to be displaced are the bridging H_2O (w_2) and O atom of Glu 227. The latter shift would move the carboxylate toward its observed position in the oxidized complex. Similar shifts in the analogous Glu ligand are proposed in metallocofactor activation of certain class Ia and class Ib O_2 s.^{8, 25-27, 30} Whereas the class Ia O_2 s are proposed to form peroxo- $\text{Fe}^{\text{III/III}}_2$ complexes after O_2 addition,^{63, 64} such a peroxo intermediate involving the Mn ion has not been observed

during activation of the Ct_2 . Addition of O_2 to the Fe site might instead yield an O_2 -superoxo- Mn^{II}/Fe^{III} complex. Attack of the Mn^{II} on the O–O unit would cleave this bond and generate the observed Mn^{IV}/Fe^{IV} intermediate directly. Crucial for this alternative mechanism is the unusually close approximation of the reduced metal ions, 3.2 Å apart, which would appropriately position the Mn^{II} ion for attack. The proposed initial mixed-valent Mn^{II}/Fe^{III} -superoxo species may be analogous to a Mn^{II}/Mn^{III} -peroxo complex recently proposed as an intermediate in activation of the class Ib $Mn_2^{II/III}$.⁹

Implications for metallocofactor biosynthesis in vivo

The factors that control in vivo metallation of class I $_2$ with Fe or Mn are not well understood. In fact, elucidation of the most active versions of the class Ib and Ic metallocofactors (including Ct_2) has been hampered by the ease with which the $_2$ scaffold can be mismetallated, especially during heterologous overexpression in *E. coli*.⁶⁵ Metallation in class Ia or Ib RNRs is most likely controlled by differential expression of proteins based on Mn^{II} or Fe^{II} availability (or perhaps metallochaperone intervention in some systems) rather than being dependent on the intrinsic metal ion affinities of a given $_2$ scaffold and its metal binding sites.⁶⁵ In class Ic RNR, use of a mixed Mn/Fe metallocofactor requires that both metals must be somewhat bioavailable for the cofactor to assemble at all. Furthermore, if the Mn^{IV}/Fe^{III} configuration is the only active form (as opposed to the Fe^{III}/Mn^{IV} arrangement), then there must be some basis to direct Mn to site 1 and Fe to site 2. The X-ray structures reported here suggest that metal ion partitioning to the appropriate site can occur during the metal-binding step. Because this happens in vitro without aid of chaperones or other accessory factors, the protein itself possesses a remarkable intrinsic metal ion binding selectivity at each site. However, the requirement for relatively strict thermodynamic and stoichiometric control of metal binding to generate homogeneous active preparations suggests that the relative levels of Mn^{II} and Fe^{II} within the cell and their order of addition in conjunction with the oxidant could be quite important in assembly of the class Ic $_2$ metallocofactor.

The basis for the intrinsic metal ion binding selectivity remains to be established, but we suggest that the unusually rigid positioning of the ligands in Ct_2 in a distorted octahedral geometry, especially at site 2, could disfavor binding of Mn^{II} to site 2 and thereby favor binding of Fe^{II} there. In our working hypothesis for in vivo metallocofactor assembly (Figure 6), Mn^{II} interacts first with the $_2$ metal binding site without preference for site 1 or site 2. Fe^{II} adds second, with a stronger affinity for site 2. This step could be facilitated by a metallochaperone or simply by limiting the available Fe^{II} within the cell to less than 1 equiv per monomer. Only with Fe^{II} bound is the protein reactive to O_2 , and activation to the exchange-inert Mn^{IV}/Fe^{III} state can then proceed. This model differs from previously proposed models, in which affinity of a specific site for Mn^{II} has been suggested to drive formation of the appropriately metallated state.^{52, 66} The use of the Mn/Fe cofactor by Ct_2 was initially rationalized as a mechanism to resist oxidative stress experienced during infection by obviating the $Y\bullet$,^{12, 42} which is known to be sensitive to nitric oxide and superoxide in the $Fe_2^{III/III}$ - $Y\bullet$ metallocofactors of class Ia RNRs.^{67, 68} Our model for class Ic metallocofactor biosynthesis suggests that use of the Mn^{IV}/Fe^{III} cofactor could, in addition, be an adaptation to Fe^{II} limitation.

The structures presented suggest a basis for the assembly of the novel heterodinuclear Mn^{IV}/Fe^{III} cofactor of Ct RNR. The structure of the apo protein reveals a metal binding site templated for selecting and activating a heterobimetallic Mn^{II}/Fe^{II} center with Mn^{II} in site 1 and Fe^{II} in site 2, but our in vitro reconstitution experiments show that this selectivity is achieved only if the divalent metals are allowed to reach their equilibrium configuration within the protein prior to exposure to O_2 . The observation that the interatomic Mn^{II} - Fe^{II} distance in the reduced cofactor (3.2 Å) is much shorter than metal-metal distances seen in

structures of homodinuclear $\text{Mn}^{\text{II}}/\text{Fe}^{\text{II}}$ and $\text{Fe}^{\text{II}}/\text{Fe}^{\text{II}}$ complexes of class Ia and Ib₂s suggests that close approximation of the two metal ions could be an adaptation to promote efficient oxidation of the $\text{Mn}^{\text{II}}/\text{Fe}^{\text{II}}$ cluster by O_2 despite the presence of the Mn^{II} , intrinsically less reducing than a second Fe^{II} . The homogeneous metallocofactor in the $\text{Mn}^{\text{II}}/\text{Fe}^{\text{II}}$ -₂ structure provides a credible starting point for computational evaluation of the O_2 -reaction coordinate in the class Ic system. The relatively small number of conformational changes seen in the structures of apo, $\text{Mn}^{\text{II}}/\text{Fe}^{\text{II}}$, and oxidized ₂ in this system may make it especially amenable to computational analysis of metallocofactor assembly. The structures additionally provide clues about in vivo assembly of a mixed-metal cofactor, suggesting that the class Ic ₂ scaffold provides a platform that can successfully assemble an active $\text{Mn}^{\text{IV}}/\text{Fe}^{\text{III}}$ center under conditions in which Mn^{II} is relatively abundant and Fe^{II} is limited.

Supplementary Material

Refer to Web version on PubMed Central for supplementary material.

Acknowledgments

Use of the Advanced Photon Source, an Office of Science User Facility operated for the U. S. Department of Energy (DOE) Office of Science by Argonne National Laboratory, was supported by the U. S. DOE under Contract No. DE-AC02-06CH11357. Use of the LS-CAT Sector 21 was supported by the Michigan Economic Development Corporation and the Michigan Technology Tri-Corridor (Grant 085P1000817). GM/CA-CAT has been funded in whole or in part with Federal funds from the National Cancer Institute (Y1-CO-1020) and the National Institute of General Medical Science (Y1-GM-1104). A.K.B. thanks Joey Cotruvo and Harry Gray for helpful discussions about Mn^{II} and Fe^{II} coordination chemistry.

Abbreviations

RNR	ribonucleotide reductase
Ct	Chlamydia trachomatis
₂	ribonucleotide reductase small subunit containing the metallocofactor
RT	radical translocation
Y•	tyrosyl radical
Ec	Escherichia coli
Bs	Bacillus subtilis
equiv	equivalents
SSM	secondary structure matching
ASU	asymmetric unit
ICP-AES	inductively coupled plasma atomic emission spectroscopy

REFERENCES

1. Stubbe J. Ribonucleotide reductases: the link between an RNA and a DNA world? *Curr. Opin. Struct. Biol.* 2000; 10:731–736. [PubMed: 11114511]
2. Nordlund P, Reichard P. Ribonucleotide reductases. *Annu. Rev. Biochem.* 2006; 75:681–706. [PubMed: 16756507]
3. Stubbe J, Nocera DG, Yee CS, Chang MCY. Radical initiation in the class I ribonucleotide reductase: long-range proton-coupled electron transfer? *Chem. Rev.* 2003; 103:2167–2201. [PubMed: 12797828]

4. Stubbe J, Ackles D. On the mechanism of ribonucleoside diphosphate reductase from *Escherichia coli*. Evidence for 3 -C--H bond cleavage. *J. Biol. Chem.* 1980; 255:8027–8030. [PubMed: 6997288]
5. Mao SS, Yu GX, Chalfoun D, Stubbe J. Characterization of C439SR1, a mutant of *Escherichia coli* ribonucleotide diphosphate reductase: evidence that C439 is a residue essential for nucleotide reduction and C439SR1 is a protein possessing novel thioredoxin-like activity. *Biochemistry.* 1992; 31:9752–9759. [PubMed: 1390751]
6. Atkin CL, Thelander L, Reichard P, Lang G. Iron and free radical in ribonucleotide reductase. Exchange of iron and Mössbauer spectroscopy of the protein 2 subunit of the *Escherichia coli* enzyme. *J. Biol. Chem.* 1973; 248:7464–7472. [PubMed: 4355582]
7. Nordlund P, Sjöberg B-M, Eklund H. Three-dimensional structure of the free radical protein of ribonucleotide reductase. *Nature.* 1990; 345:593–598. [PubMed: 2190093]
8. Cox N, Ogata H, Stolle P, Reijerse E, Auling G, Lubitz W. A tyrosyl-dimanganese coupled spin system is the native metalloradical cofactor of the R2F subunit of the ribonucleotide reductase of *Corynebacterium ammoniagenes*. *J. Am. Chem. Soc.* 2010; 132:11197–11213. [PubMed: 20698687]
9. Cotruvo JA Jr, Stich TA, Britt RD, Stubbe J. Mechanism of assembly of the dimanganese-tyrosyl radical cofactor of class Ib ribonucleotide reductase: Enzymatic generation of superoxide is required for tyrosine oxidation via a Mn(III)Mn(IV) intermediate. *J. Am. Chem. Soc.* 2013; 135:4027–4039. [PubMed: 23402532]
10. Cotruvo JA Jr, Stubbe J. An active dimanganese(III)-tyrosyl radical cofactor in *Escherichia coli* class Ib ribonucleotide reductase. *Biochemistry.* 2010; 49:1297–1309. [PubMed: 20070127]
11. Bollinger JM Jr, Edmondson DE, Huynh BH, Filley J, Norton JR, Stubbe J. Mechanism of assembly of the tyrosyl radical-dinuclear iron cluster cofactor of ribonucleotide reductase. *Science.* 1991; 253:292–298. [PubMed: 1650033]
12. Jiang W, Yun D, Saleh L, Barr EW, Xing G, Hoffart LM, Maslak MA, Krebs C, Bollinger JM Jr. A manganese(IV)/iron(III) cofactor in *Chlamydia trachomatis* ribonucleotide reductase. *Science.* 2007; 316:1188–1191. [PubMed: 17525338]
13. Jiang W, Hoffart LM, Krebs C, Bollinger JM Jr. A manganese(IV)/iron(IV) intermediate in assembly of the manganese(IV)/iron(III) cofactor of *Chlamydia trachomatis* ribonucleotide reductase. *Biochemistry.* 2007; 46:8709–8716. [PubMed: 17616152]
14. Jiang W, Saleh L, Barr EW, Xie J, Gardner MM, Krebs C, Bollinger JM Jr. Branched activation- and catalysis-specific pathways for electron relay to the manganese/iron cofactor in ribonucleotide reductase from *Chlamydia trachomatis*. *Biochemistry.* 2008; 47:8477–8484. [PubMed: 18656954]
15. Bollinger JM Jr, Jiang W, Green MT, Krebs C. The manganese(IV)/iron(III) cofactor of *Chlamydia trachomatis* ribonucleotide reductase: structure, assembly, radical initiation, and evolution. *Curr. Opin. Struct. Biol.* 2008; 18:650–657. [PubMed: 19046875]
16. Högbom M. The manganese/iron-carboxylate proteins: what is what, where are they, and what can the sequences tell us? *J. Biol. Inorg. Chem.* 2010; 15:339–349. [PubMed: 20225400]
17. Jiang W, Bollinger JM Jr, Krebs C. The active form of *Chlamydia trachomatis* ribonucleotide reductase R2 protein contains a heterodinuclear Mn(IV)/Fe(III) cluster with S = 1 ground state. *J. Am. Chem. Soc.* 2007; 129:7504–7505. [PubMed: 17530854]
18. Jiang W, Xie J, Nørgaard H, Bollinger JM Jr, Krebs C. Rapid and quantitative activation of *Chlamydia trachomatis* ribonucleotide reductase by hydrogen peroxide. *Biochemistry.* 2008; 47:4477–4483. [PubMed: 18358006]
19. Jiang W, Xie J, Varano PT, Krebs C, Bollinger JM Jr. Two distinct mechanisms of inactivation of the class Ic ribonucleotide reductase from *Chlamydia trachomatis* by hydroxyurea: implications for the protein gating of intersubunit electron transfer. *Biochemistry.* 2010; 49:5340–5349. [PubMed: 20462199]
20. Younker JM, Krest CM, Jiang W, Krebs C, Bollinger JM Jr, Green MT. Structural analysis of the Mn(IV)/Fe(III) cofactor of *Chlamydia trachomatis* ribonucleotide reductase by extended X-ray absorption fine structure spectroscopy and density functional theory calculations. *J. Am. Chem. Soc.* 2008; 130:15022–15027. [PubMed: 18937466]

21. Dassama LMK, Boal AK, Krebs C, Rosenzweig AC, Bollinger JM Jr. Evidence that the beta subunit of *Chlamydia trachomatis* ribonucleotide reductase is active with the manganese ion of its manganese(IV)/iron(III) cofactor in site 1. *J. Am. Chem. Soc.* 2012; 134:2520–2523. [PubMed: 22242660]
22. Andersson CS, Öhrström M, Popovi -Bijeli A, Gräslund A, Stenmark P, Högbom M. The manganese ion of the heterodinuclear Mn/Fe cofactor in *Chlamydia trachomatis* ribonucleotide reductase R2c is located at metal position 1. *J. Am. Chem. Soc.* 2012; 134:123–125. [PubMed: 22133609]
23. Åberg A, Nordlund P, Eklund H. Unusual clustering of carboxyl side chains in the core of iron-free ribonucleotide reductase. *Nature.* 1993; 361:276–278. [PubMed: 8423856]
24. Högbom M, Huque Y, Sjöberg B-M, Nordlund P. Crystal structure of the di-iron/radical protein of ribonucleotide reductase from *Corynebacterium ammoniagenes*. *Biochemistry.* 2002; 41:1381–1389. [PubMed: 11802741]
25. Boal AK, Cotruvo JA Jr, Stubbe J, Rosenzweig AC. Structural basis for activation of class Ib ribonucleotide reductase. *Science.* 2010; 329:1526–1530. [PubMed: 20688982]
26. Boal AK, Cotruvo JA Jr, Stubbe J, Rosenzweig AC. The dimanganese(II) site of *Bacillus subtilis* class Ib ribonucleotide reductase. *Biochemistry.* 2012; 51:3861–3871. [PubMed: 22443445]
27. Voegtli WC, Sommerhalter M, Saleh L, Baldwin J, Bollinger JM Jr, Rosenzweig AC. Variable coordination geometries at the diiron(II) active site of ribonucleotide reductase R2. *J. Am. Chem. Soc.* 2003; 125:15822–15830. [PubMed: 14677973]
28. Eriksson M, Jordan A, Eklund H. Structure of *Salmonella typhimurium* NrdF ribonucleotide reductase in its oxidized and reduced forms. *Biochemistry.* 1998; 37:13359–13369. [PubMed: 9748343]
29. Logan DT, Su XD, Åberg A, Regnström K, Hajdu J, Eklund H, Nordlund P. Crystal structure of reduced protein R2 of ribonucleotide reductase: the structural basis for oxygen activation at a dinuclear iron site. *Structure.* 1996; 4:1053–1064. [PubMed: 8805591]
30. Nordlund P, Eklund H. Structure and function of the *Escherichia coli* ribonucleotide reductase protein R2. *J. Mol. Biol.* 1993; 232:123–164. [PubMed: 8331655]
31. The class Ib and Ic O_2 proteins can form O_2 -reactive $\text{Fe}^{\text{II/II}}_2$ clusters in vitro or when overexpressed in a heterologous host. However, these clusters are either inactive (class Ic *CtRNR*) or less active and apparently not utilized in vivo (all class Ib RNRs isolated from their native organisms to date).
32. Otwinowski Z, Minor W. Processing of X-ray diffraction data collected in oscillation mode. *Methods Enzymol.* 1997; 276:307–326.
33. McCoy AJ, Grosse-Kunstleve RW, Storoni LC, Read RJ. Likelihood-enhanced fast translation functions. *Acta Crystallogr.* 2005; D61:458–464.
34. Murshudov GN, Vagin AA, Dodson EJ. Refinement of macromolecular structures by the maximum-likelihood method. *Acta Crystallogr.* 1997; D53:240–255.
35. Emsley P, Cowtan K. Coot: model-building tools for molecular graphics. *Acta Crystallogr.* 2004; D60:2126–2132.
36. Schrödinger, LLC. The PyMOL Molecular Graphics System. 2010
37. Krissinel E, Henrick K. Secondary-structure matching (SSM), a new tool for fast protein structure alignment in three dimensions. *Acta Crystallogr.* 2004; D60:2256–2268.
38. Ten Eyck LF. Fast Fourier transform calculation of electron density maps. *Methods Enzymol.* 1985; 115:324–337. [PubMed: 3841183]
39. Than ME, Henrich S, Bourenkov GP, Bartunik HD, Huber R, Bode W. The endoprotease furin contains two essential Ca^{2+} ions stabilizing its N-terminus and the unique S1 specificity pocket. *Acta Crystallogr.* 2005; D61:505–512.
40. Chen VB, Arendall WB III, Headd JJ, Keedy DA, Immormino RM, Kapral GJ, Murray LW, Richardson JS, Richardson DC. MolProbity: all-atom structure validation for macromolecular crystallography. *Acta Crystallogr.* 2010; D66:12–21.
41. Zwart PH, Afonine PV, Grosse-Kunstleve RW, Hung LW, Ioerger TR, McCoy AJ, McKee E, Moriarty NW, Read RJ, Sacchettini JC, Sauter NK, Storoni LC, Terwilliger TC, Adams PD.

- Automated structure solution with the PHENIX suite. *Methods Mol. Biol.* 2008; 426:419–435. [PubMed: 18542881]
42. Högbom M, Stenmark P, Voevodskaya N, McClarty G, Gräslund A, Nordlund P. The radical site in chlamydial ribonucleotide reductase defines a new R2 subclass. *Science.* 2004; 305:245–248. [PubMed: 15247479]
 43. Vonrhein C, Blanc E, Roversi P, Bricogne G. Automated structure solution with autoSHARP. *Methods Mol. Biol.* 2007; 364:215–230. [PubMed: 17172768]
 44. The procedure utilized for generating Fe-specific anomalous maps is not quantitative and underestimates the quantity of Fe present at a given site because it fails to account for the decay in Mn absorption with decreasing wavelength away from the Mn edge. Therefore, we report quantification of only the Mn anomalous signal in Table 1. Estimates for Fe occupancies are reported in Table S9.
 45. Yang YS, Baldwin J, Ley BA, Bollinger JM Jr, Solomon EI. Spectroscopic and electronic structure description of the reduced binuclear non-heme iron active site in ribonucleotide reductase from *E. coli*: Comparison to reduced ⁹ desaturase and electronic structure contributions to differences in O₂ reactivity. *J. Am. Chem. Soc.* 2000; 122:8495–8510.
 46. Sigfridsson KG, Chernev P, Leidel N, Popovi -Bijeli A, Gräslund A, Haumann M. Rapid X-ray photoreduction of dimetal-oxygen cofactors in ribonucleotide reductase. *J. Biol. Chem.* 2013; 288:9648–9661. [PubMed: 23400774]
 47. The data for Mn^{II} in site 1 are modeled best with 85-95% metal ion occupancy, and the data for Fe^{II} at site 2 by 100% occupancy. The slightly diminished occupancy of Mn^{II} at site 1 may be significant, possibly reflecting a difference in affinities.
 48. Atta M, Nordlund P, Åberg A, Eklund H, Fontecave M. Substitution of manganese for iron in ribonucleotide reductase from *Escherichia coli*. *J. Biol. Chem.* 1992; 267:20682–20688. [PubMed: 1328209]
 49. Whittington DA, Lippard SJ. Crystal structures of the soluble methane monooxygenase hydroxylase from *Methylococcus capsulatus* (Bath) demonstrating geometrical variability at the dinuclear iron active site. *J. Am. Chem. Soc.* 2001; 123:827–838. [PubMed: 11456616]
 50. Sazinsky MH, Lippard SJ. Correlating structure with function in bacterial multicomponent monooxygenases and related diiron proteins. *Acc. Chem. Res.* 2006; 39:558–566. [PubMed: 16906752]
 51. Krebs C, Bollinger JM Jr, Booker SJ. Cyanobacterial alkane biosynthesis further expands the catalytic repertoire of the ferritin-like ‘di-iron-carboxylate’ proteins. *Curr. Opin. Chem. Biol.* 2011; 15:291–303. [PubMed: 21440485]
 52. Cotruvo JA, Stubbe J. Class I ribonucleotide reductases: metallocofactor assembly and repair in vitro and in vivo. *Annu. Rev. Biochem.* 2011; 80:733–767. [PubMed: 21456967]
 53. Meharena YT, Doukov T, Li H, Soltis SM, Poulos TL. Crystallographic and single-crystal spectral analysis of the peroxidase ferryl intermediate. *Biochemistry.* 2010; 49:2984–2986. [PubMed: 20230048]
 54. Zhang Y, Stubbe J. *Bacillus subtilis* class Ib ribonucleotide reductase is a dimanganese(III)-tyrosyl radical enzyme. *Biochemistry.* 2011; 50:5615–5623. [PubMed: 21561096]
 55. Orgel, LE. An introduction to transition-metal chemistry: ligand-field theory. 2nd Ed.. Wiley; New York: 1966. p. 59-64.
 56. Hayden JA, Brophy MB, Cunden LS, Nolan EM. High-affinity manganese coordination by human calprotectin is calcium-dependent and requires the histidine-rich site formed at the dimer interface. *J. Am. Chem. Soc.* 2013; 135:775–787. [PubMed: 23276281]
 57. Damo SM, Kehl-Fie TE, Sugitani N, Holt ME, Rathi S, Murphy WJ, Zhang Y, Betz C, Hench L, Fritz G, Skaar EP, Chazin WJ. Molecular basis for manganese sequestration by calprotectin and roles in the innate immune response to invading bacterial pathogens. *Proc. Natl. Acad. Sci. USA.* 2013; 110:3841–3846. [PubMed: 23431180]
 58. Antonyuk SV, Melik-Adamyanyan VR, Popov AN, Lamzin VS, Hempstead PD, Harrison PM, Artymyuk PJ, Barynin VV. Three-dimensional structure of the enzyme dimanganese catalase from *Thermus thermophilus* at 1 angstrom resolution. *Crystallogr. Rep.* 2000; 45:105–116.

59. Li J, Fisher CL, Chen JL, Bashford D, Noodleman L. Calculation of redox potentials and pK_a values of hydrated transition metal cations by a combined density functional and continuum dielectric theory. *Inorg. Chem.* 1996; 35:4694–4702.
60. Williams RJP. Energised (entatic) states of groups and of secondary structures in proteins and metalloproteins. *Eur. J. Biochem.* 1995; 234:363–381. [PubMed: 8536678]
61. Strumm, G.; Morgan, JJ. *Aquatic Chemistry*. Wiley; New York: 1996. p. 445p. 672-690.
62. Andersson ME, Högbom M, Rinaldo-Matthis A, Andersson KK, Sjöberg B-M, Nordlund P. The crystal structure of an azide complex of the diferrous R2 subunit of ribonucleotide reductase displays a novel carboxylate shift with important mechanistic implications for diiron-catalyzed oxygen activation. *J. Am. Chem. Soc.* 1999; 121:2346–2352.
63. Tong WH, Chen S, Lloyd SG, Edmondson DE, Huynh BH, Stubbe J. Mechanism of assembly of the diferric cluster-tyrosyl radical cofactor of *Escherichia coli* ribonucleotide reductase from the diferrous form of the R2 subunit. *J. Am. Chem. Soc.* 1996; 118:2107–2108.
64. Yun D, García-Serres R, Chicalese BM, An YH, Huynh BH, Bollinger JM Jr. (μ -1,2-peroxo)diiron(III/III) complex as a precursor to the diiron(III/IV) intermediate X in the assembly of the iron-radical cofactor of ribonucleotide reductase from mouse. *Biochemistry.* 2007; 46:1925–1932. [PubMed: 17256972]
65. Cotruvo JA Jr, Stubbe J. Metallation and mismetallation of iron and manganese proteins in vitro and in vivo: the class I ribonucleotide reductases as a case study. *Metallomics.* 2012; 4:1020–1036. [PubMed: 22991063]
66. Han WG, Giammona DA, Bashford D, Noodleman L. Density functional theory analysis of structure, energetics, and spectroscopy for the Mn-Fe active site of *Chlamydia trachomatis* ribonucleotide reductase in four oxidation states. *Inorg. Chem.* 2010; 49:7266–7281. [PubMed: 20604534]
67. Roy B, Lepoivre M, Henry Y, Fontecave M. Inhibition of ribonucleotide reductase by nitric oxide derived from thionitrites: reversible modifications of both subunits. *Biochemistry.* 1995; 34:5411–5418. [PubMed: 7727399]
68. Gaudu P, Nivière V, Petillot Y, Kauppi B, Fontecave M. The irreversible inactivation of ribonucleotide reductase from *Escherichia coli* by superoxide radicals. *FEBS Lett.* 1996; 387:137–140. [PubMed: 8674535]

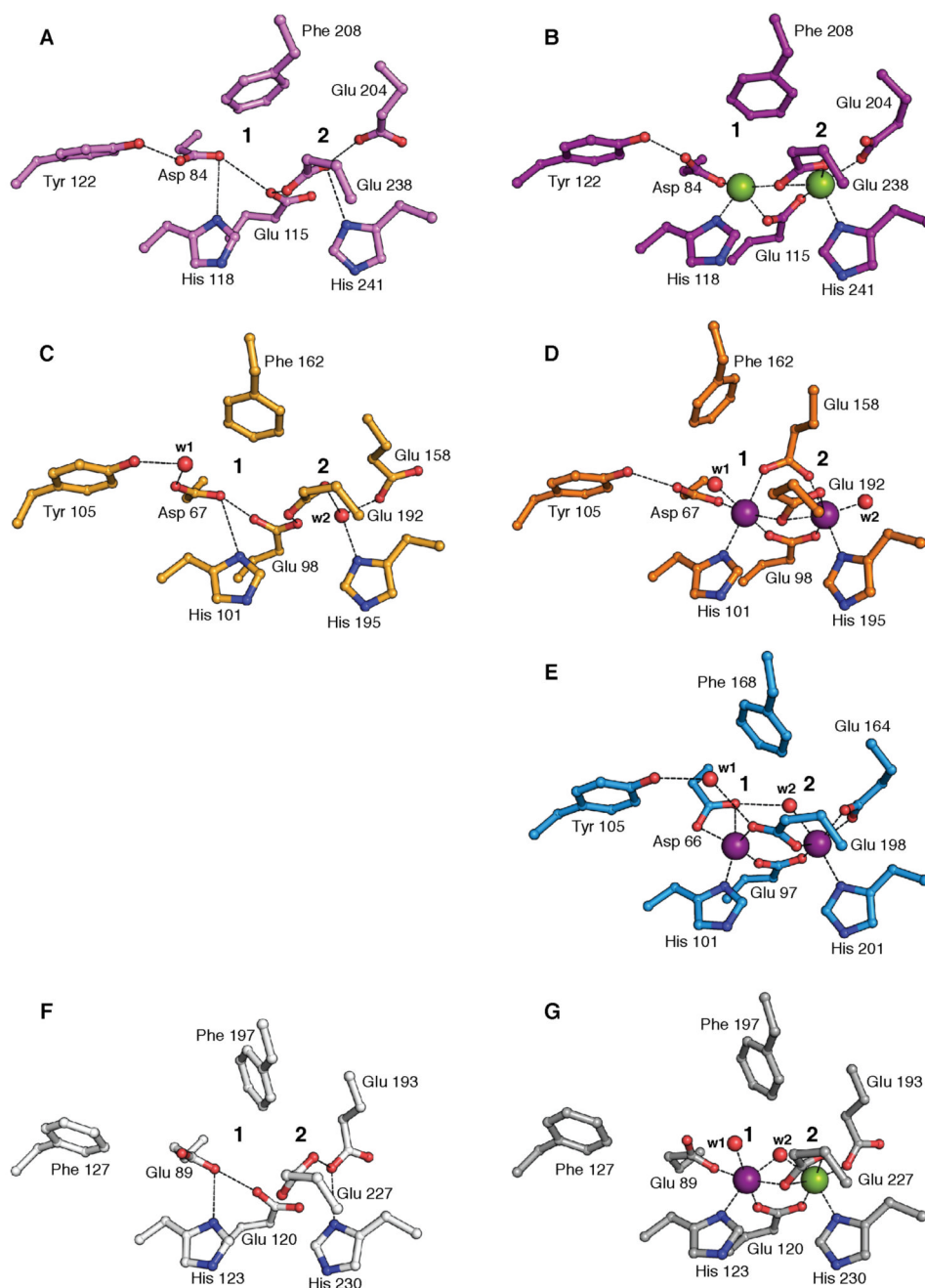


Figure 1.

Comparison of the apo and reduced metallocofactor sites in class I heme proteins. (A) *Ec* class Ia apo Fe^{II} site (PDB accession code 1PIY), (B) *Ec* class Ia Fe^{II} site (PDB accession code 1PIY), (C) *Ec* class Ib apo Mn^{II} site (PDB accession code 4M1F), (D) *Ec* class Ib Mn^{II} site (PDB accession code 3N38), (E) *Bs* class Ib Mn^{II} site (PDB accession code 4DR0), (F) *Ct* class Ic apo Mn^{II} site, and (G) *Ct* class Ic Mn^{II} site. Ligands and selected outer sphere residues are shown as sticks. Mn^{II} and Fe^{II} ions are shown as purple and green spheres, respectively. Ordered water molecules are shown as red spheres. Metal-ligand interactions and selected hydrogen bonds are shown as gray dashed lines.

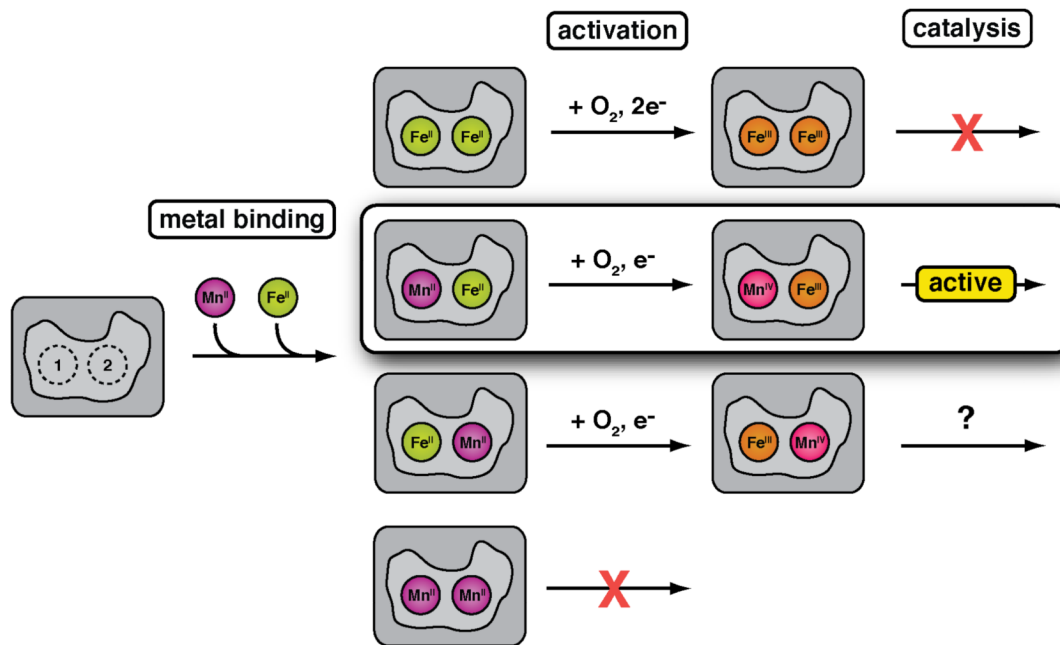


Figure 2. Schematic depiction of productive and unproductive steps during the *in vitro* assembly of the Mn/Fe metallocofactor in *Ct*₂. In the metal-binding step, four possible cluster types can be assembled. Mn^{II}/Mn^{II} clusters do not react with O₂. Fe^{II}/Fe^{II} clusters react with O₂ to form Fe^{III}/Fe^{III} clusters that are inactive in nucleotide reduction. Mn^{II}/Fe^{II} and Fe^{II}/Mn^{II} clusters can both react with O₂, and it is possible that each may be competent to initiate nucleotide reduction. However, the data presented here and previously²¹ suggest the Mn^{II}/Fe^{II} form is the relevant precursor to the active cofactor.

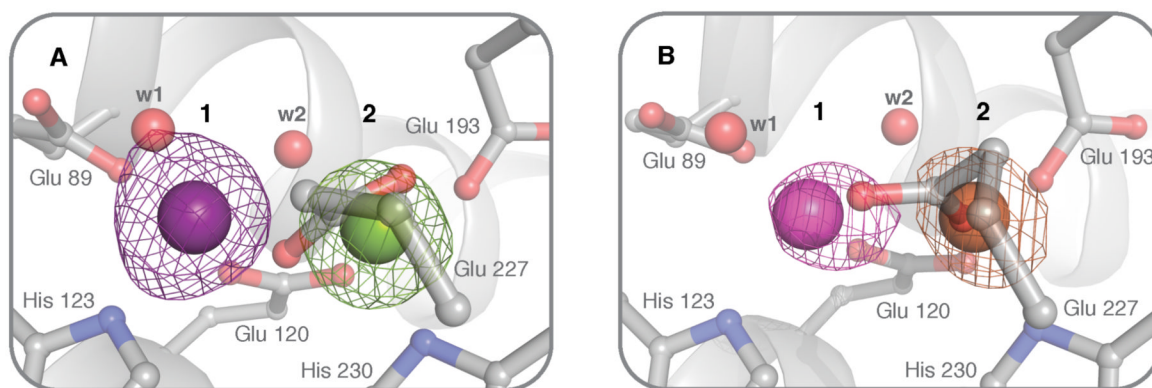


Figure 3.

Metal site assignment from the anomalous X-ray scattering by Mn and Fe ions in crystals of *Ct*₂. Selected active site residues are shown in stick format. Metal ions and water molecules are shown as spheres. Mn is present in site 1 and Fe in site 2, and anomalous difference density is not observed above background (5.0-6.0 σ) in the opposite site for either metal. **(A)** From crystals of Mn^{II}/Fe^{II}-₂ obtained by loading apo-₂ with 1 equiv of each metal per monomer followed by anaerobic crystallization, anomalous difference maps were obtained for both Mn (purple mesh) and Fe (green mesh) and are shown contoured at 6.0 σ . **(B)** Samples of Mn^{IV}/Fe^{III}-₂ for crystallization were prepared by procedure 3B (anaerobic loading of 1 equiv each Mn^{II} and Fe^{II} per monomer followed by O₂ exposure; see Table 2). From the resultant crystals, anomalous difference maps were obtained for Mn (pink mesh) and Fe (orange mesh) and are shown contoured at 5.0 σ .

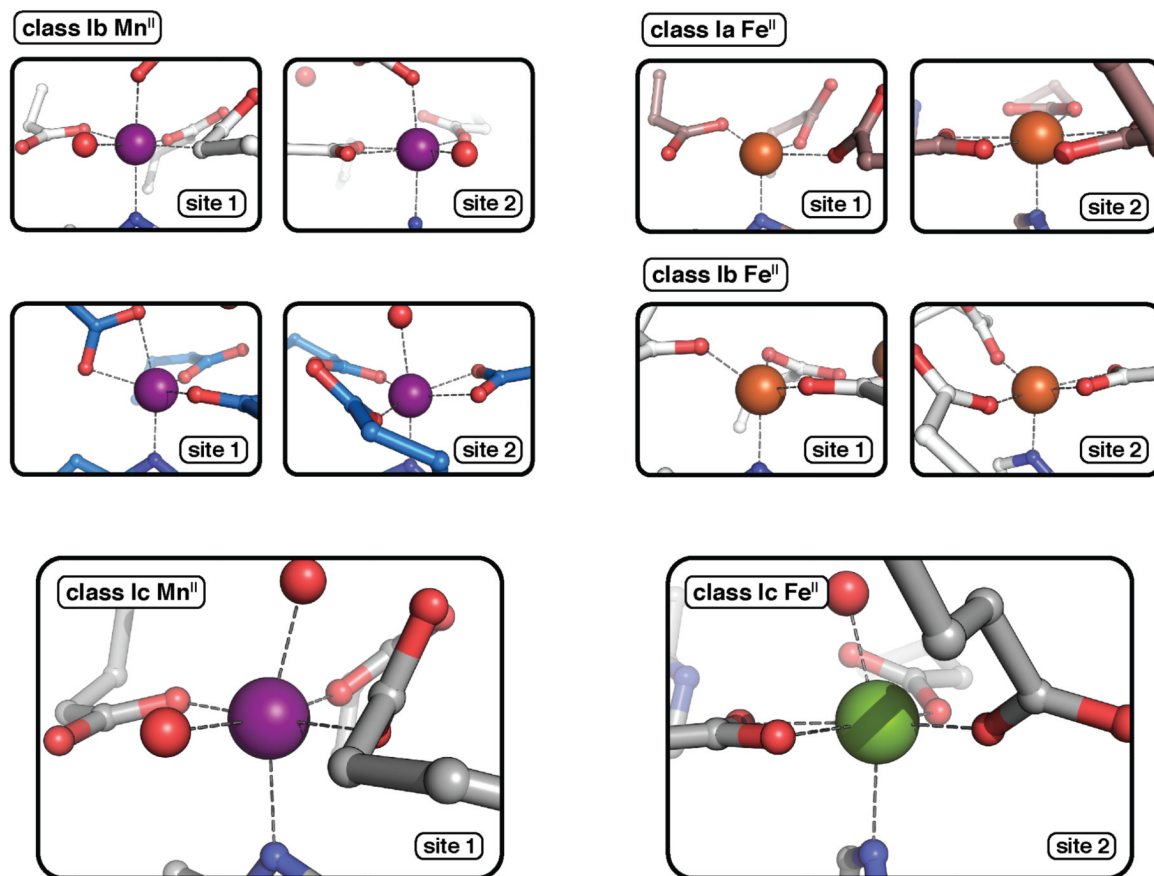


Figure 5.

Representative Mn^{II} and Fe^{II} coordination geometries in class I RNRs. Class Ia $\text{Fe}^{\text{II}}_{2-2}$ (PDB accession code 1PIY) and class Ib $\text{Fe}^{\text{II}}_{2-2}$ (PDB accession code 3N38) structures were used to generate the Fe^{II} panels at top left. Class Ib $\text{Mn}^{\text{II}}_{2-2}$ structures from the *Ec* (white, PDB accession code 3N37) and *Bs* (blue, PDB accession code 4DR0) enzymes were used to generate the Mn^{II} panels at top right. Note that the Mn^{II} sites in the class Ib $_{2-2}$ structures tend to exhibit higher coordination numbers with more strict adherence to octahedral geometry than the Fe^{II} coordination environments in the class Ia or Ib $_{2-2}$ s. This trend is more apparent in the class Ib *Ec* $\text{Mn}^{\text{II}}_{2-2}$ structure than in the class Ib *Bs* $\text{Mn}^{\text{II}}_{2-2}$, and interestingly, the *Ec* protein binds Mn^{II} more tightly than the *Bs* homolog.⁹ Shown at bottom is a comparison to the coordination environments in class Ic $_{2-2}$ at site 1 (Mn^{II} , left) and site 2 (Fe^{II} , right). The binding sites in class Ic $_{2-2}$ resemble those in the Mn^{II} structures from class Ib $_{2-2}$ s in that they are six-coordinate with exogenous water ligands, but the geometric distortion, particularly axial to the His ligand, is similar to $\text{Fe}^{\text{II}}_{2-2}$ metal-binding interactions.

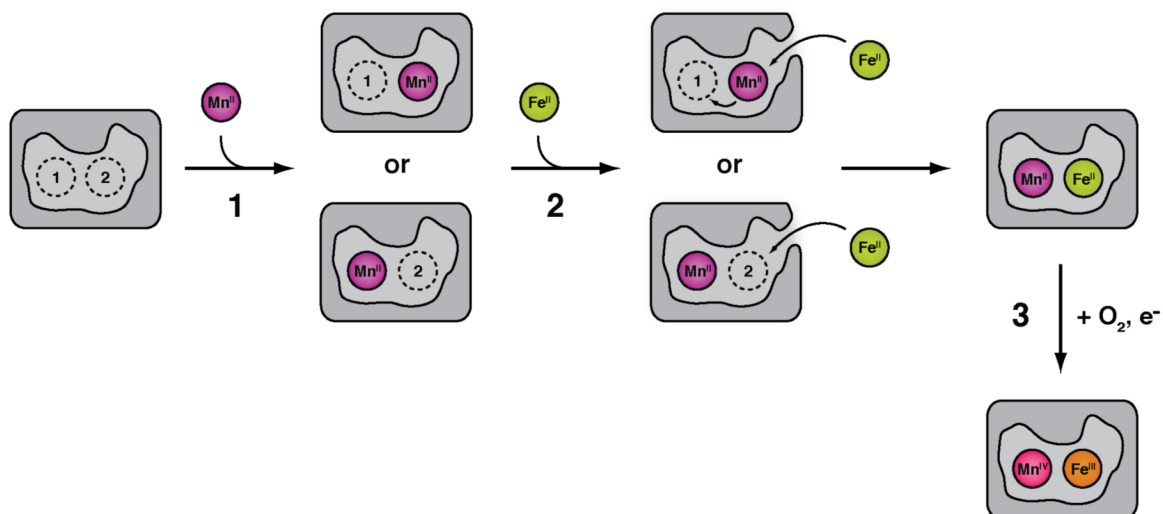


Figure 6.

A model for in vivo cofactor assembly in the α_2 subunit of *Ct* class Ic RNR. In step 1, Mn^{II} ion is taken up by the apo protein first with little to no preference for site 1 or site 2. In the second step, Fe^{II} ions bind selectively to site 2. The preference of site 2 for Fe^{II} could be controlled in part by the rigid, distorted six-coordinate geometry of the α_2 metal binding sites. In vivo, site specificity could be enhanced by the action of a chaperone delivering Fe^{II} to site 2 via a specific pathway. Reaction with the oxidant occurs in step 3. The model posits that the preference of Fe^{II} for site 2 drives formation of the Mn^{II}/Fe^{II} cluster in preference to the Fe^{II}/Mn^{II} form to ensure efficient production of the more active Mn^{IV}/Fe^{III} state.

Table 1

Anomalous peak heights () at the Mn absorption edge for Ct_2 crystallographic datasets.

Crystal	Chain	Site 1	Site 2
Mn^{II}/Fe^{II}-₂	A	18.3	4.0
	B	14.9	4.1
	C	14.7	5.0
	D	14.7	2.1
Mn^{IV}/Fe^{III}-₂ procedure-3A	A	13.1	2.4
	B	8.6	3.7
	C	11.5	3.5
	D	5.6	2.4
Mn^{IV}/Fe^{III}-₂ procedure-3B	A	6.3	--
	B	7.6	--
	C	5.3	1.4
	D	4.0	--

Table 2Metal incorporation (equiv per) and enzymatic activity analysis for Mn^{IV}/Fe^{III}-₂.

Preparation	Mn ^{II} added	Fe ^{II} added	Mn retained	Fe retained	v/ (s ⁻¹)	v/Mn (s ⁻¹)
procedure-3A	2.0	0.65	0.40	0.42	0.50	1.16
procedure-3B	1.0	1.0	0.48	0.68	0.56	1.25
procedure-3C	0.65	2.0	0.38	1.26	0.48	1.24
procedure-1 ^a	1.50	0.75	0.55	0.65	0.38	0.70
procedure-2 ^a	0.15	1.0	0.13	0.73	0.16	1.10

^aAs reported in ref. 21.